The International Journal of Advanced Manufacturing Technology (2020) 108:1931–1944
https://doi.org/10.1007/s00170-020-05492-7

ORIGINAL ARTICLE

Theoretical study on the effects of the axial and radial runout and tool corner radius on surface roughness in slot micromilling process

Tao Wang[1,2] · Xiaoyu Wu[1] · Guoqing Zhang[1] · Bin Xu[1] · Yinghua Chen[1] · Shuangchen Ruan[2]

Received: 2 February 2020 / Accepted: 15 May 2020 / Published online: 3 June 2020

Abstract
This paper presented a theoretical study on the effects of the axial and radial runout and tool corner radius on surface roughness in the slot micromilling process. Firstly, the actual feed rate was calculated based on the optimized model for the uncut chip thickness. Then, the milled morphologies in five typical cases are analyzed, and the details of the flowchart for the modeling process are drawn, and the corresponding surface morphology and surface roughness are presented. Next, the effects of radial runout offset and angle, axial offset, and tool corner radius on surface roughness were studied. Furthermore, three typical surface morphologies, i.e., a single cutting phenomenon, unbalanced cutting phenomena due to the radial runout and axial runout, were obtained from the slot micromilling experiment, which could verify the validity of the model indirectly. In the end, the approaches for improving the predicting accuracy were discussed. The findings could provide a better understanding of the surface formation process during slot micromilling process.

Keywords Micromilling · Runout · Surface morphology · Surface roughness · Uncut chip thickness

Abbreviation

R_1	The rotational radius of tooth 1 (μm)
R_2	The rotational radius of tooth 2 (μm)
R	The nominal radius of the milling tool (μm)
r_0	The radial runout offset (μm)
λ	The radial runout angle
K	The number of the flutes
k	The flute number
n	The spindle velocity (rev/min)
f_t	The feed rate (μm/z)
t	Time (s)
h_1	Uncut chip thickness of the Nie's model (μm)
h_2	Uncut chip thickness of the Bao's model (μm)
h_3	Uncut chip thickness of the Wan's model (μm)
φ_i	Cutter rotation angle (rad)
m	The current tooth i is removing the material left by the mth previous tooth
$R_{i,j}(z)$	Actual cutting radii of the jth axial disk element of the ith flute at z (μm)
h_a	Actual feed rate (μm/z)

✉ Xiaoyu Wu
wuxy@szu.edu.cn

[1] Guangdong Provincial Key Laboratory of Micro/Nano Optomechatronics Engineering, College of Mechatronics and Control Engineering, Shenzhen University, Nan-hai Ave. 3688, Shenzhen 518060, Guangdong, China

[2] Key Laboratory of Optoelectronic Devices and Systems of Ministry of Education and Guangdong Province, College of Optoelectronic Engineering, Shenzhen University, Shenzhen 518060, China

1 Introduction

Due to its wide material choices, low cost, 3D microgeometry machining capability, and high accuracy, the slot micromilling is recognized as one of the most versatile machining techniques to fabricate microcomponents and microfeatures [1–3]. Predicting surface morphology of a milled surface could help engineers to choose appropriate inputs, e.g., milling parameters, and tool geometry, before the actual experiment, which draws great attention in both the academic and industrial fields in recent decades [4]. Ideally, the surface profile of the milled workpiece is generated by the repetition of the milling tool-tip geometry at the spatial interval of the feed. However, the ideal pattern could be compromised by many factors in the actual milling process, among

which the radial and axial runout and tool corner radius are significant items. In order to achieve the required surface roughness, a comprehensive understanding of the factors that influence surface roughness is essential.

Some empirical approaches are utilized to predict the surface roughness, which could achieve a satisfactory accuracy. Based on the experimental results, Singh et al. [5] studied the influence of cutting conditions and tool geometries on the finished surface roughness during hard turning of the bearing steel and established a model for predicting surface roughness by response surface methodology (RSM). Palanikumar et al. [6] used Taguchi method and RSM to model the surface roughness in machining the glass fiber-enforced plastics. Wang et al. [7] used the RSM to predict the surface roughness in high-speed milling of Al/SiC/65p. However, one disadvantage in using empirical approaches is that the predicted surface roughness depends heavily on the process parameters, which can be easily affected by the random errors. Besides, it is hard to provide explicit analysis based on the empirical model [8].

To avoid the weakness of empirical method, it is important to understand the surface generation mechanism in micromachining. Rahman et al. [9] proposed a mathematical model for the material removal mechanism with relation to edge radius effect. The model was able to capture the trend of the change of surface generation mechanism from shearing to extrusion to plowing and rubbing. The corresponding orthogonal cutting experiments were conducted for the validation of the results. Then, many theoretical approaches have been explored in predicting surface roughness in turning process. Based on analyzing the effect of both the relative vibration and the swelling, Chen and Zhao [10] proposed a model to predict surface roughness R_a in single-point diamond turning (SPDT) based on analyzing both the relative vibration and the swelling effect. Lee and Cheung [11] established a dynamic surface topography model to predict the material-induced vibration and its effect on the surface generation in SPDT. Wang et al. [12] proposed a geometric model with the effect of tool-tip vibration to identify the dominant factors in the calculation of nanometric surface roughness. The tool-tip vibration and the process damping effect are regarded as the prime influences on surface roughness. Liu et al. [13] built a model for predicting the surface roughness in microturning of Al5083-H116 alloy, which consider the effects of tool geometry, plastic side flow, and process parameters. They found that the discrepancy between the measured and theoretical surface roughness in microturning could be mainly attributed to the surface roughening caused by plastic side flow. Zong et al. [14] established a comprehensive model to predict the surface roughness achieved by single-point diamond turning; the model considered the effects of the plastic side flow, the minimum uncut chip thickness, and the material elastic recovery and swelling. From the theoretical models above, the main influential factors of the turned surface roughness include the material crystallographic orientation, the material elastic recovery and swelling, machining parameters, tool geometry, and the minimum uncut chip thickness.

Although the theoretical methods for predicting surface roughness have been explored comprehensively, the majority of the above reporters focused on the study of the surface roughness in turning process. In the micromilling process, Wojciechowski et al. [15] found that the chip thickness accumulation, the kinematics, radial runout, elastic and plastic deformations of workpiece correlated with the minimum uncut chip thickness, and flexibility of the slender microend mill could all influence the milling process. As for size effect, Oliveira et al. [16] studied it in different milling scales by analyzing the behavior of the specific cutting force when varying feed per tooth and depth of cut. The results indicated that any MCT varied between 1/4 and 1/3 of the tool edge radius, regardless of the workpiece material. The majority of the published papers about the influence of the runout in the micromilling process focused on the runout measuring method [17–19] and the influence of the runout on the micromilling force [20, 21]. Recently, some researchers studied the influence of runout on surface morphology and roughness in the micromilling process. Sun et al. [22] established a 2D model of surface generation in micromilling process based on the minimum cutting thickness and cutter geometry, but the influence of runout is omitted. Li et al. [23] established a surface roughness model based on tool wear, minimum chip thickness, and microtool geometry in micromilling process, which is verified with experimental results. The influence of runout was neglected either. Kim et al. [24] built a surface prediction numerical model for microend milling which included the non-dynamic errors of microend milling such as tool geometric and set-up errors (tool eccentricity, tilted edge part, and tool runout). Although the predicted results had a very similar variation trend with the experimental results, the huge gap was observed between the predicted and experimental results. Chen et al. [25] proposed a surface generation model for microend milling process, in which the effect of the minimum chip thickness (MCT) and tool runout is considered. The results indicated that the model with MCT and tool runout has a high prediction accuracy over a wide range of feed rates, but the radial runout is simplified as $r\cdot(-1)^{i+1}$. Chen et al. [26] presented a surface generation simulation in microend milling considering both axial and radial tool runout. They found that the axial runout has a significant influence on the surface topography generation. The model was used to predict the single tooth cutting phenomenon successfully. However, the influence of axial and radial runout on surface roughness is not investigated in the paper. Besides, the influence of the radial runout angle is neglected. As for the influence of the tilt angle of the spindle on the generated surface roughness and morphology, Aurich et al. [27] studied them based on kinematic simulations and experiments in micromilling

process. When a tilted spindle was set, C- or D-tracks could be generated, thereby increasing surface roughness. Besides, burr formation could be minimized by choosing appropriate tilt angles of the main spindle.

As been mentioned above, the majority of the reported surface models mainly consider the influence of the radial runout, the minimum chip thickness, tool geometry, and feed rate on the surface profile. However, to the best of the authors' knowledge, incorporating the effect of both axial and radial runout (offset and angle) and the tool radius on the milled surface morphology and roughness in the slot micromilling process has rarely been explored in the literature before. The purpose of the paper is to demonstrate the relationship between the radial and axial runout and tool corner radius on surface morphology and surface roughness. It could provide guidance for choosing the appropriate parameters in the slot micromilling process. The simulation in the paper is based on purely kinematic modeling which does not consider any material properties.

2 Modeling process

2.1 The runout model

Runout of the cutting tool is a common phenomenon in the slot micromilling process. The radial runout is generated when the microtool center deviates from the spindle axis due to the eccentricity of the tool-holder-spindle assembly. It can lead to the difference in the rotational radiuses of each tool flute. The radial runout can be defined by a runout offset r_0 and a runout angle λ [17], as shown in Fig. 1a. O is the rotational center of the holder-spindle axis, and O′ is the microtool center.

Based on the geometric relationship, the rotational radiuses of tooth 1 and tooth 2 can be calculated by the formula as below:

$$\begin{cases} R_1 = \sqrt{R^2 + r_0^2 - 2Rr_0\cos(\pi-\lambda)} \\ R_2 = \sqrt{R^2 + r_0^2 - 2Rr_0\cos(\lambda)} \end{cases} \quad (1)$$

The calculated R_1 and R_2 under different radial runout offsets and angles are shown in Fig. 1 b and c, respectively. R is set as 497.56 μm The R_1 is larger than R_2 as the radial runout angle is below 90°, while the scenario reverses when the radial runout angle increases over 90°. The gap between the two radiuses is shown in Fig. 1d. The absolute maximum value occurs at runout offset 5 μm and runout angle 0 or 180°. Besides, when the runout angle is 90°, the difference reduces to 0.

When axial runout occurs, one tooth touches the workpiece more than the other during the slot micromilling process, thereby wearing more quickly. It is usually generated when the tool tilts to the spindle axis due to the error in the tool-holder-spindle assembly. Besides, the different tool wear conditions can lead to the axial runout as well. It has a significant influence on the formation process of surface morphology [26]. The axial runout offset is defined as r_a in the paper.

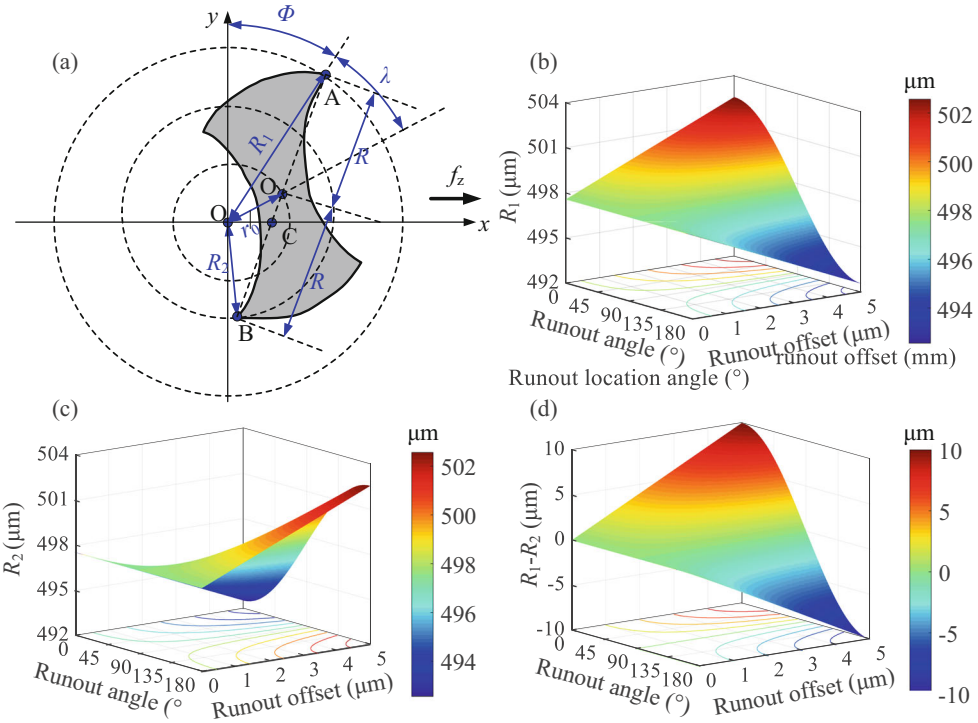

Fig. 1 The analysis of the radial runout phenomenon for a two-tooth milling tool. **a** The schematic diagram of the radial runout. **b** The influence of runout offset and angle on the high tooth radius R_1. **c** The influence of runout offset and angle on the low tooth radius R_2. **d** The influence of runout offset and angle on the difference between R_1 and R_2

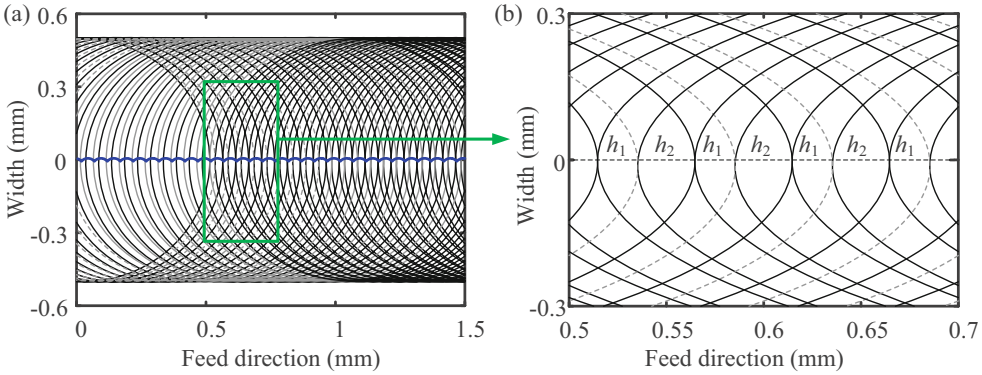

Fig. 2 The trajectory of the two-tooth tips in the micromilling process. **a** The macrotrajectory. **b** The enlarged image from the macrotrajectory

2.2 The calculation of the actual feed rate

Obtaining the actual feed rate is the foundation for modeling surface morphology. The trajectory of the kth tool tip in the slot micromilling can be given as

$$\begin{cases} x = nKf_t/60 + R\sin(2\pi nt/60 - 2\pi k/K) + r_0\sin(2\pi nt/60 + \lambda) \\ y = R\cos(2\pi nt/60 - 2\pi k/K) + r_0\cos(2\pi nt/60 + \lambda) \end{cases} \tag{2}$$

where f_t is the feed rate (μm/z), n is the spindle velocity (rev/min), t is time (s), k is the flute number, K is the number of flutes, r_0 is the runout length (mm), and λ is the runout angle (rad).

Correspondingly, the trajectory of the two tool tips in slot micromilling process can be drawn in Fig. 2. The feed rate is set large to demonstrate the trajectory clearly.

According to the literature, three general models for calculating the uncut chip thickness in the cylindrical end milling process are listed as below:

1. Nie's model [28]

$$h_1 = f_t\left(1 - \frac{\delta}{\pi}\right)\sin\varphi_i + 2r_0\cos\lambda - r_0\delta\sin\lambda + R\frac{\delta^2}{2} \tag{3}$$

where

$$\delta = \frac{f_t\cos\varphi_i + 2r_0\sin\lambda}{R} \tag{4}$$

2. Bao's model [29]

$$h_2 = f_t\left[1 + (-1)^k\frac{2r_0}{\pi R}\sin\lambda\right]\sin\theta - \frac{1}{\pi R}f_t^2\sin\theta\cos\theta + \frac{1}{2r}f_t^2\cos^2\theta - (-1)^z 2r_0\cos\lambda \tag{5}$$

3. Wan's model [30]

$$h_3 = \min_{m=1}^{N}\left\{mf\sin\theta_{i,1}(\varphi_k) + R^r_{i,1}(z) - R^r_{i-m,1}(z)\right\} \tag{6}$$

where

$$R_{i,j}(z) = R(z) + r_0\cos[\lambda - 2(i-1)\pi/N] \tag{7}$$

In the meantime, a numerical calculation method is proposed in [3] based on the Newton–Raphson (N-R) iterative method. The depths of cut calculated by the four models at different rotation angle is shown in Fig. 3. Generally, the predicted depths by the four models are consistent. Assuming the depth $h_{\text{N-R}}$ predicted by the numerical calculation method is more accurate, it is set as the benchmark. The enlarged image of Zone A and Zone B, as shown in Fig. 3a and c, demonstrates that the depth predicted by Bao's model located on the line of the N-R method, while the other two results deviate from the curve of the N-R method. Besides, the relative errors of the top three models from the benchmark are shown in Fig. 4. The

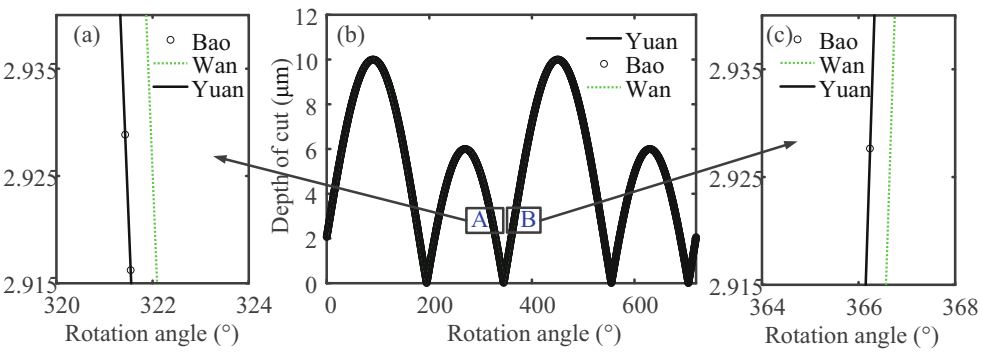

Fig. 3 The predicted uncut chip thickness by the three models. **a** The enlarged image of zone A. **b** The predicted uncut chip thickness. **c** The enlarged image of zone B. (Simulation conditions: $R = 500$ μm, $f_z = 8$ μm/z, $r_0 = 1$ μm)

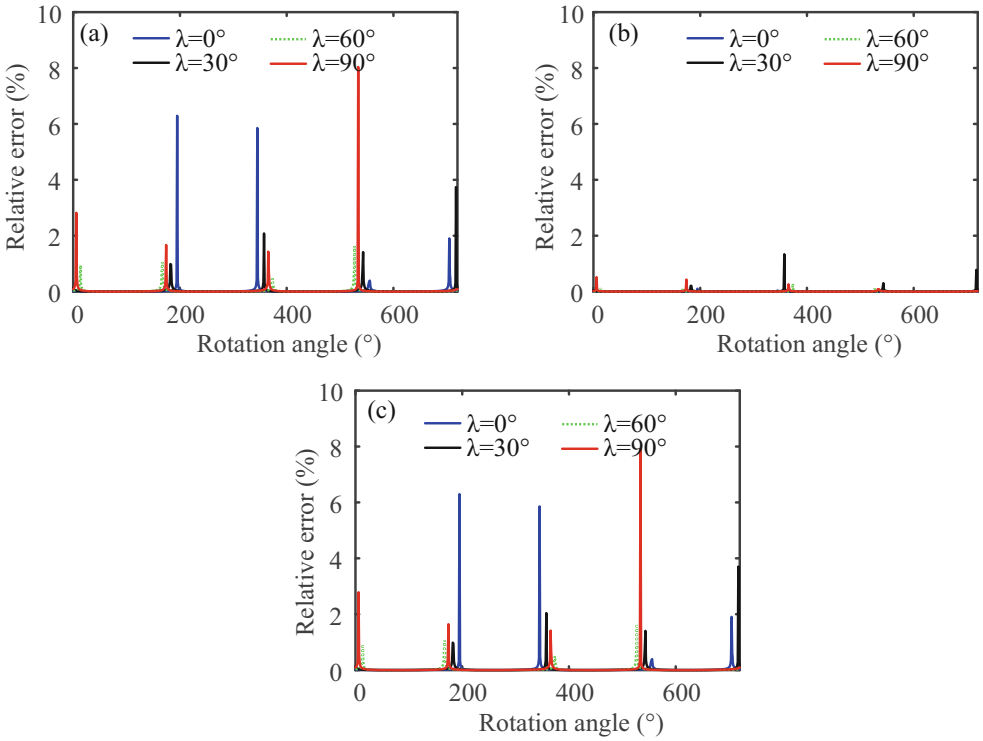

Fig. 4 The relative error results. **a** h_1-$h_{N\text{-}R}$. **b** h_2-$h_{N\text{-}R}$. **c** h_3-$h_{N\text{-}R}$. (Simulation conditions: R = 500 μm, f_z = 8 μm/z, r_0 = 1 μm)

results indicate that the relative errors of the top three models are negligible at the majority of rotation angle range except for the area around $(n-1)180°$ (n = 1, 2, 3 ….). Among the three models, the error of Bao's model is the minimum.

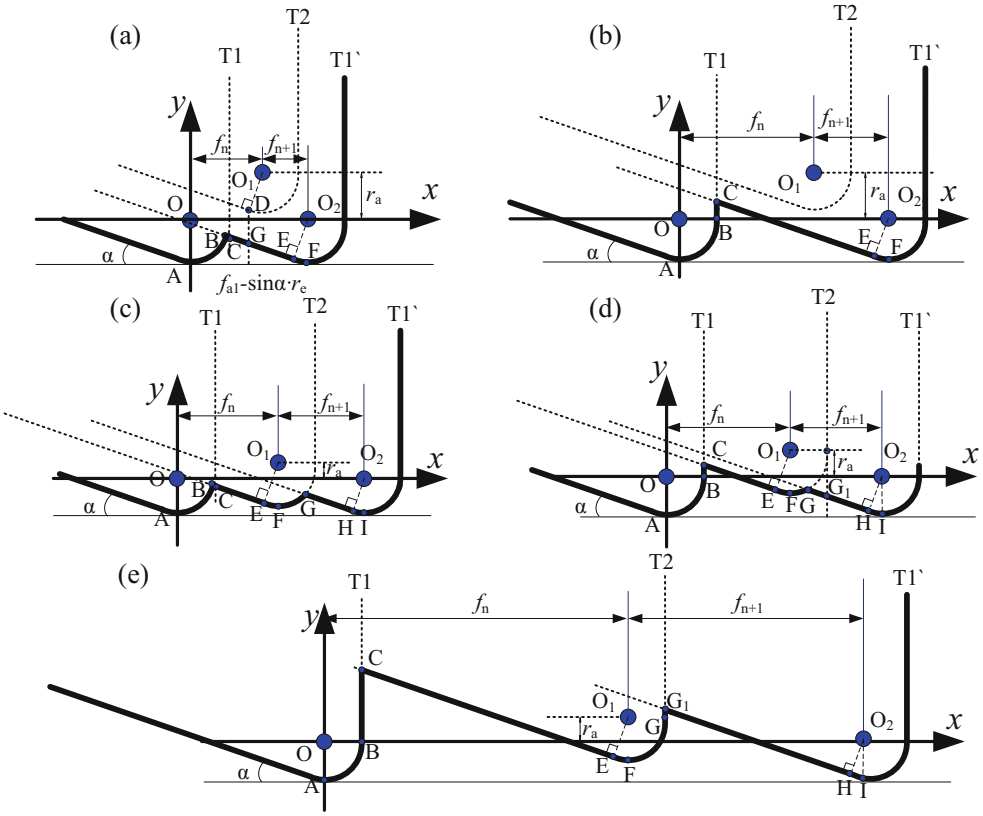

Fig. 5 The schematic diagram of the surface formation processes. **a** Case 1: the T1 arc intersects with the T1′ line (single tooth cutting). **b** Case 2: the T1 line intersects with the T1′ line (single tooth cutting). **c** Case 3: the T1 arc intersects with the T2 line and the T2 arc intersects with T1′ line. **d** Case 4: the T1 line intersects with the T2 line and the T2 arc intersects with T1′ line. **e** Case 5: the T1 line intersects with the T2 line and the T2 line intersects with T1′ line

Therefore, the Bao's model is utilized to predict the uncut chip thickness in the paper. Since all the channel in the study is generated by the full-immersion slot micromilling process, the actual feed rate at the centerline of the bottom channel can be calculated at rotation angle $\theta = \mathrm{pi}/2 + (n-1)*\mathrm{pi}$ ($n = 1, 2, 3\ldots$). According to Eq. (4), the actual feed rate is formulated as below:

$$h_a = f_t + (-1)^z 2r_0\left(\frac{\sin\lambda}{\pi R} f_t - \cos\lambda\right) \tag{8}$$

2.3 The modeling process of the micromilled surface morphology

Under different runout conditions, the surface morphologies generated by the tool cutting edge in one rotation circle are shown in Fig. 5. Generally, the morphology can be classified based on the intersection point location. If cutting edge T1 does not intersect with T2 after one feed distance, single-tooth cutting phenomenon occurs, as shown in Fig. 5a and b. Afterward, if the intersection point between T1 and T1′ locates on the arc AB, it is defined as case 1; otherwise, it is defined as case 2. If cutting edge T1 intersects with T2, based on the location of the intersection point, it can be classified into other three cases as shown in Fig. 5c, d, and e, respectively. The details of the surface morphology modeling process are shown in Figs. 6 and 7.

Figure 8 demonstrates the predicted surface morphologies of the five cases. The left image is macrochannel morphology generated in the milling process. To provide a clear image of a local region, an area in the channel center is enlarged as shown in middle. The corresponding profiles can be extracted from the 3D model, and the surface roughness can be calculated based on the data of the profiles. According to Fig. 8, the established model has a good capability to predict surface morphology and surface roughness.

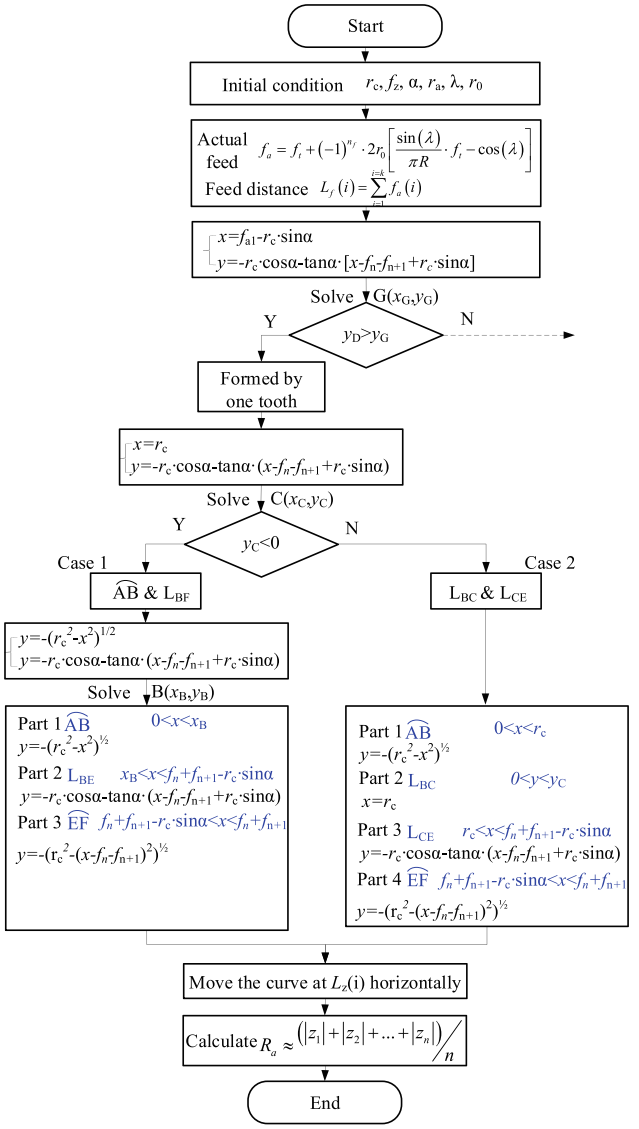

Fig. 6 The flowchart 1–1 of the surface morphology modeling process for the single-tooth cutting phenomenon (The whole process is consisted of three parts: setting initial conditions, calculating the coordinates of intersection points, and calculating the surface roughness)

3 The results from the established model

3.1 Influence of radial runout offset and angle

Based on the measurement results from [3, 20, 22] in the slot micromilling process, the runout value r_0 is usually from 1 to 3 μm, and it is set as the range of the radial runout length in this section. The radial runout offset is set as $r_0 = 0{:}0.2{:}3$, and the radial runout angle is set as $\lambda = 0{:}5°{:}180°$. The established model is utilized to calculate the surface roughness under 528 runout conditions. The results are fitted linearly, and the corresponding contour is shown in Fig. 9. The maximum roughness occurs at the top right and bottom right corner, and the image is symmetric along the horizontal line at runout angle 90°. The surface roughness increases with the radial runout offset. The surface roughness decreases with the increase of runout angle when the runout angle is below 90°, while the scenario reverses when the runout angle is above 90°.

3.2 Influence of axial runout

The influence of axial runout on surface roughness is shown in Fig. 10. In Fig. 10a, the surface roughness is predicted under different combinations of $r_a = [0{:}0.1{:}0.7]$ μm and $r_0 = [0{:}0.2{:}3]$ μm, and then the results are fitted linearly to form the contour. It is interesting to find that surface roughness increases with the radial runout offset and axial offset. However, in the upper right corner filled with yellow, the

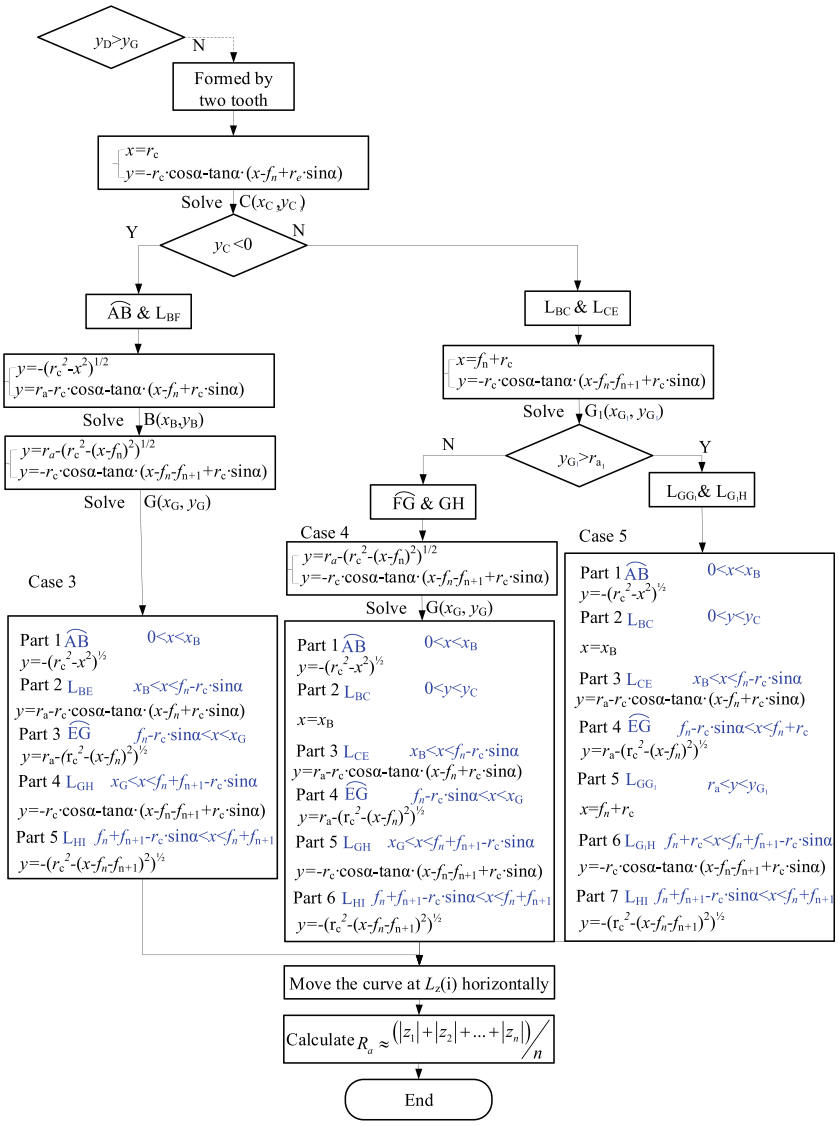

Fig. 7 The flowchart 1–2 of the surface morphology modeling process for the two-teeth cutting phenomenon

influence of the radial runout offset and axial offset on surface roughness vanishes. To explore the reason, the corresponding surface profiles under the five colorful points are drawn in Fig. 11a. When the radial runout offset is below 2 μm, the two-tooth cutting phenomenon occurs in one rotation cycle, while as it increases to 2 μm and 2.5 μm, the single-tooth cutting phenomenon happens in one rotation cycle. Therefore, under the single-tooth cutting scenario, the influence of the radial runout offset and axial offset can be neglected.

In Fig. 10b, the surface roughness is predicted under different combinations of $r_a = [0{:}0.1{:}0.7]$ μm and $\lambda = [0{:}20°{:}180°]$, and then the results are fitted linearly to form the contour. The minimum surface roughness is around the zone with a low axial runout offset and a 90° radial runout angle. The surface roughness increases with the axial runout offset as well. At the upper left corner filled with yellow, the influence of the radial runout angle and axial offset on surface roughness vanishes. It can also be attributed to the occurrence of a single-tooth cutting phenomenon. The corresponding surface profiles under the colorful point conditions are shown in Fig. 11b.

3.3 Influence of tool corner radius

The influence of the corner radius on surface roughness is shown in Fig. 12. In Fig. 12a, the surface roughness is predicted under different combinations of $r_c = [1.35, 5, 10, 15, 20]$ μm and $r_0 = [0{:}0.5{:}3]$ μm, and then the results are fitted linearly to form the contour. The maximum surface roughness zone is at the bottom right corner, which means that the smaller corner radius and larger radial runout offset can get higher surface roughness. The surface profiles under the five colorful points are shown in Fig. 13a. It can be observed that the larger

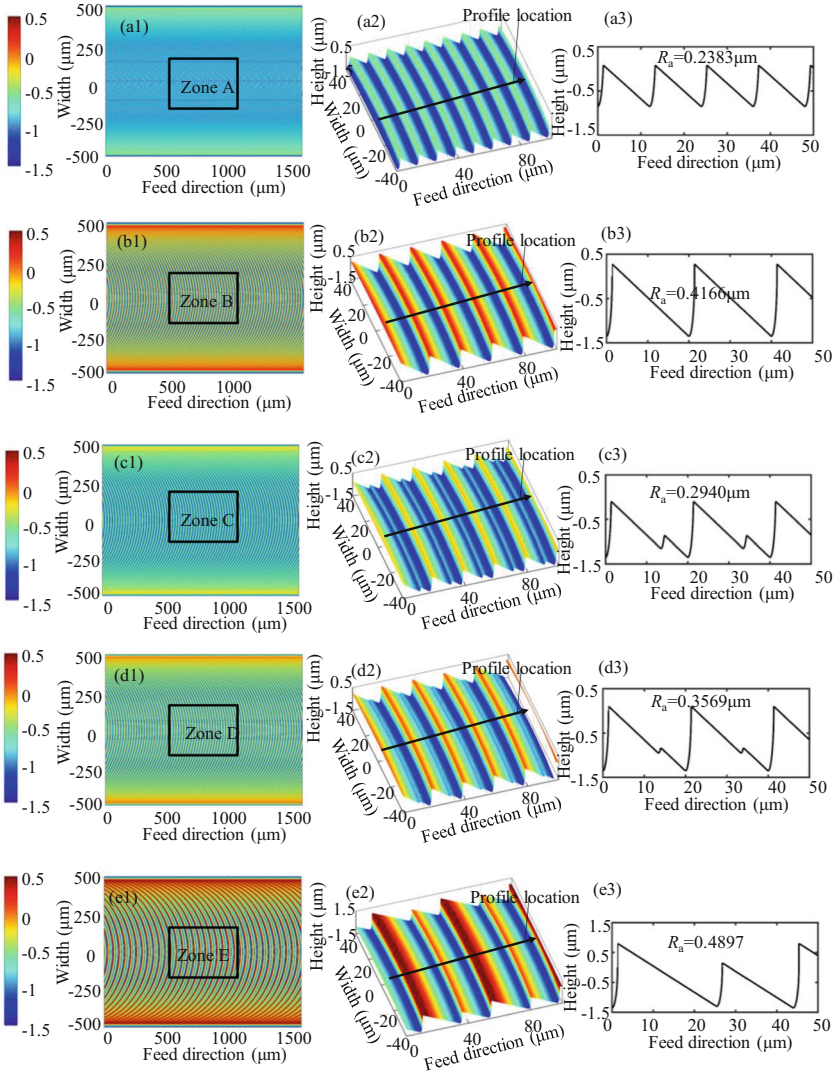

Fig. 8 The predicted surface morphology of the five cases. **a** Case 1: $f_t = 6$ μm/z, $r_0 = 2$ μm, $\lambda = 30$, $r_a = 0.4$ μm, $r_c = 1.35$ μm. **b** Case 2: $f_t = 10$ μm/z, $r_0 = 2$ μm, $\lambda = 30$, $r_a = 1$ μm, $r_c = 1.35$ μm. **c** Case 3: $f_t = 10$ μm/z, $r_0 = 2$ μm, $\lambda = 30$, $r_a = 0.2$ μm, $r_c = 1.35$ μm. **d** Case 4: $f_t = 10$ μm/z, $r_0 = 2$ μm, $\lambda = 30$, $r_a = 0.4$, $r_c = 1.35$ μm. **e** Case 5: $f_t = 22$ μm/z, $r_0 = 2$ μm, $\lambda = 30$, $r_a = 0.05$, $r_c = 1.35$ μm

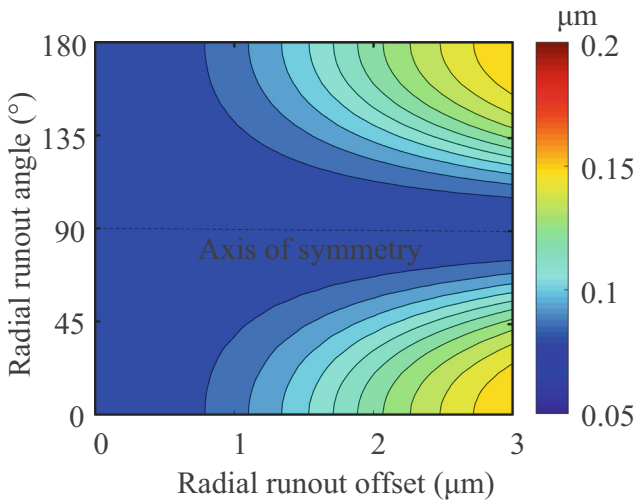

Fig. 9 The influence of radial runout offset and angle on surface roughness (milling conditions: $f_t = 8$ μm, $R = 497.56$ μm, $\alpha = 2.5°$, $r_a = 0$ μm, $r_a = 1.35$ μm)

corner radius can reduce the height of the peak to valley, thereby reducing the surface roughness.

In Fig. 12b, the surface roughness is predicted under different combinations of $r_a = [0{:}0.1{:}0.7]$ μm and $r_c = [1.35,5,10,15,20]$ μm, and then the results are fitted linearly to form the contour. When the axial runout offset is below 0.2 μm, the trend is similar to that in Fig. 12a, and the maximum surface roughness is at the bottom right corner. The surface roughness increase with the increase of the axial runout offset and the decrease of the corner radius. When the axial runout offset is above 0.2 μm, the influence of the axial runout offset vanishes. The corresponding surface profiles under the five colorful points are drawn as shown in Fig. 13b. It indicates that when the axial runout offset is above 0.2 μm, the single cutting phenomenon occurs, and the influence of the axial runout offset can be neglected, and the surface roughness only decreases with the increase of the corner radius.

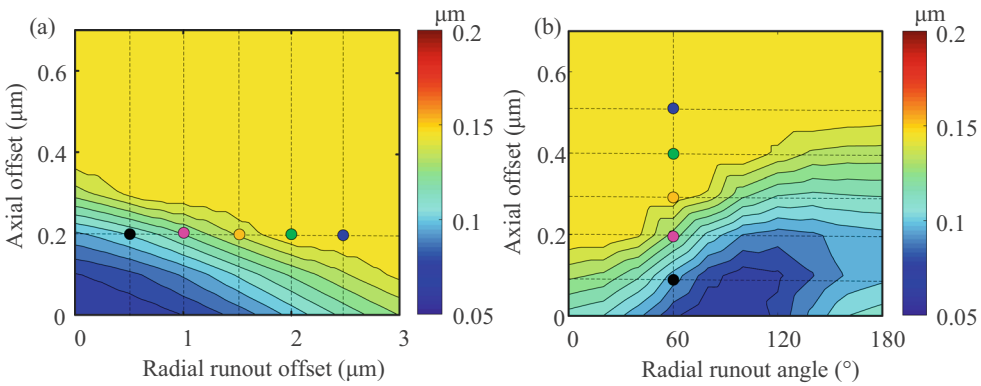

Fig. 10 The contours of the surface roughness. **a** The influence of the axial runout offset r_a and the radial runout offset r_0 at $\lambda = 30°$. **b** The influence of the axial runout offset r_a and the radial runout angle λ at $r_0 = 2$ μm. (Simulation conditions: $f_t = 8$ μm, $R = 497.56$ μm, $\alpha = 2.5°$, $r_c = 5$ μm)

4 Experimental morphology verification

Due to that the lack of the measuring instruments for the radial and axial runout are in the lab currently, the actual comparisons of surface roughness between the experimental and predicted results are not presented in the paper. However, the slot micromilling surface morphology generated in the experiment clearly demonstrated that the variation in the surface profile cannot only be attributed to the feed marks. Three typical phenomena are found, which could be explained by the established model, thereby verifying the model indirectly.

4.1 Experimental setup

The slot micromilling tests are conducted on the DMU CNC machining center, and the setup is shown in Fig. 14a. In order to avoid the occurrence of the chatter, the axial depth of cut is set to be below 50 μm [31]; therefore, the influence of chatter is neglected. To minimize the deflection effect, the distance to the tool tip from the tool-holder (overhang length) was fixed at 20 mm during the experiments [32]. The workpiece is Zr-based bulk metallic glass ($Zr_{41.2}Ti_{13.8}Cu_{12.5}Ni_{10}Be_{22.5}$), provided by Tongji University. The cemented carbide milling tools coated with TiAlN and CrN provided by NT Tool. The tool diameter is 995.12 μm, and rake angle and helix angle are 12° and 30°, respectively. The cutting edge radius r_e and nose radius r_c is 2.56 μm and 1.35 μm, respectively. The morphology of the tool is shown in Fig. 14b–d. The 3D pseudo photo and profiles of the milled surfaces were detected by a profiler (Contour GT-X white light interferometer, Bruker).

4.2 Surface morphology from the milled surface in slot micromilling experiment

Different slot micromilling tests were conducted, and three typical milled surface morphologies were picked, as shown in Fig. 15, 16, and 17. Figure 15 demonstrates a single cutting phenomenon. The feed rate is 1.5 μm/z, while the pitch of the profile is close to 3 μm. Neglecting the influence of axial runout, Li et al. [20] proposed a criterion for the single tooth cutting phenomenon as below:

$$\varepsilon = f_t - |2r_0 \cos \lambda| \tag{9}$$

when $\varepsilon < 0$, the single-tooth cutting phenomenon occurs.

From the results in Fig. 10, even the radial runout parameters can guarantee $\varepsilon > 0$, if the axial runout varies, the single-

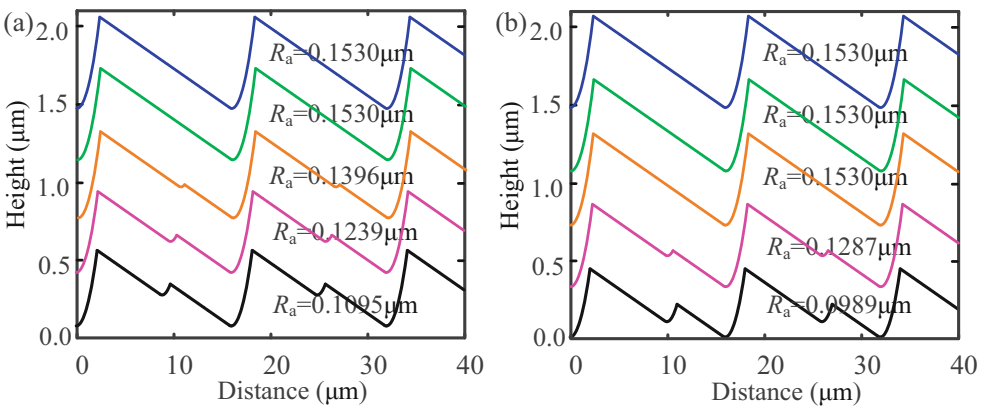

Fig. 11 The corresponding surface profiles at colorful points in Fig. 10. **a** The profiles at variable radial runout offset and fixed axial runout offset $r_a = 0.2$ μm. **b** The profiles at variable axial runout offset and fixed radial runout angle $\lambda = 60°$

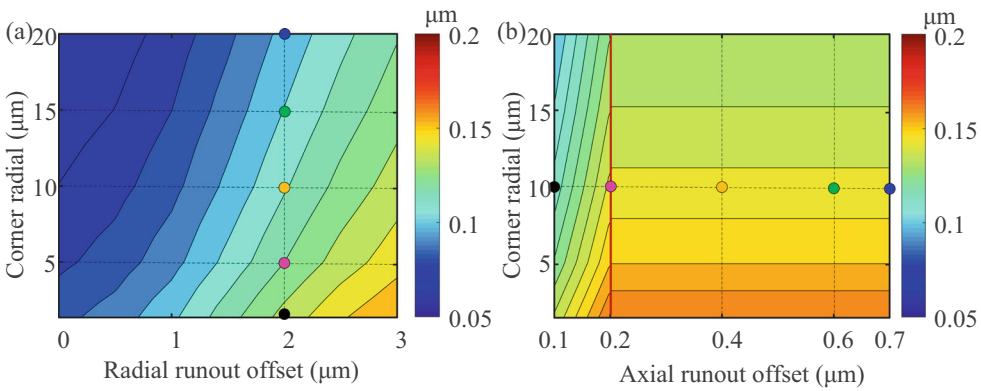

Fig. 12 The contours of the surface roughness. **a** The influence of the radial runout offset r_0 and the corner radius r_c at $r_a = 0.1$ μm. **b** The influence of the axial runout offset r_a and the corner radius r_c at $r_0 = 2$ μm. (simulation conditions: $f_t = 8$ μm, $R = 497.56$ μm, $\alpha = 2.5°$, $\lambda = 30°$)

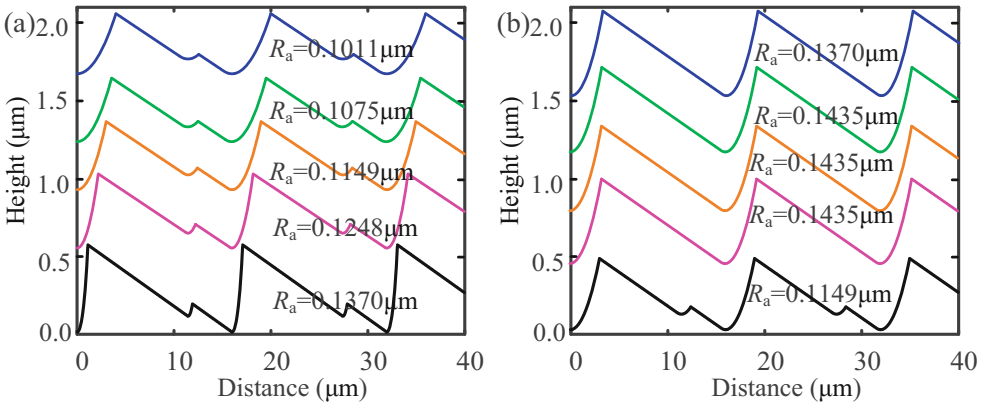

Fig. 13 The corresponding surface profiles at colorful points in Fig. 12. **a** The profiles at variable corner radius and fixed radial runout offset $r_0 = 2$ μm. **b** The profiles at variable axial runout offset and fixed corner radius $r_c = 10$ μm

tooth cutting phenomenon can occur as well. Therefore, considering the influence of axial and radial runout simultaneously, based on the geometry relationship (Fig. 5) and the flowchart (Fig. 6), a more comprehensive criterion is proposed as below:

$$\varepsilon_N = y_D - y_G = r_a - \tan\alpha \cdot \left[f_t + 2r_0 \cdot \left(\frac{\sin\lambda \cdot f_t}{\pi R} - \cos\lambda \right) \right] \quad (10)$$

when $\varepsilon_N > 0$, single-tooth cutting phenomenon occurs. To make sure if the single-tooth cutting phenomenon is merely generated by radial runout or by both axial and radial runout, the corresponding runout parameters should be obtained in advance.

The unbalanced cutting phenomena due to the radial runout and axial runout are demonstrated in Figs. 16 and 17, respectively. The formation mechanism can both be explained by the established model in the paper, which indirectly verifies the validity of the model successfully.

5 Discussion

It is worth pointing out that the surface roughness calculated in the paper is the ideal value, and it is assuming that the workpiece experiences pure plastic deformation in the slot micromilling process. In reality, there are many factors

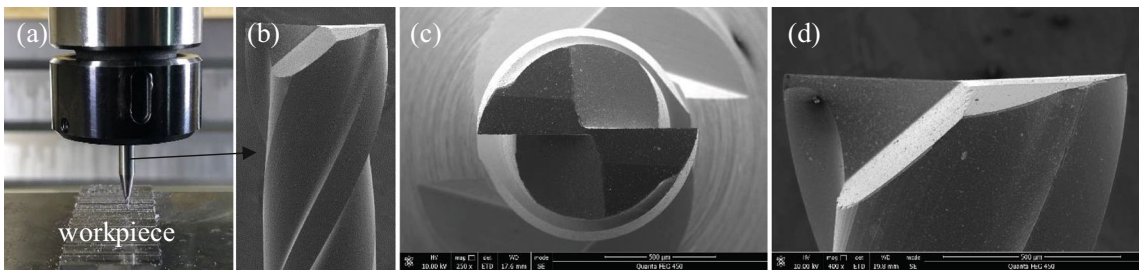

Fig. 14 The experimental setup and tool morphology. **a** Experimental setup. **b** Macro view of the micromilling tool. **c** Top view of the micromilling tool. **d** Side view of the micromilling tool

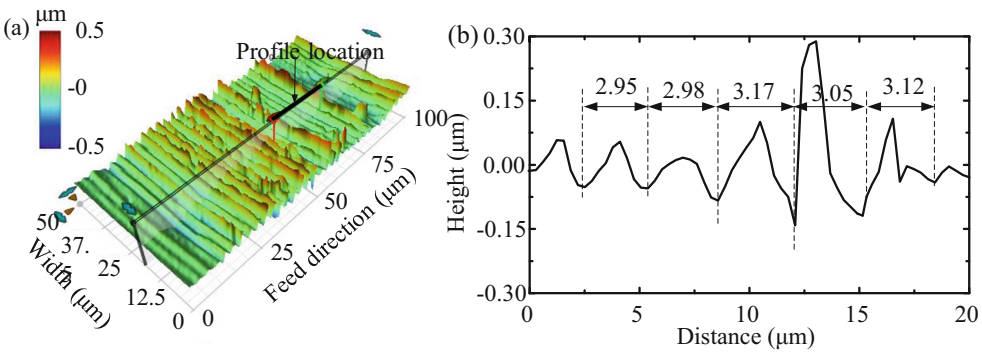

Fig. 15 A single-tooth cutting phenomenon. **a** The 3D morphology of the milled surface. **b** The extracted profile. (milling conditions: $n = 10{,}000$ rpm, $a_p = 45$ μm, $f_z = 1.5$ μm/z)

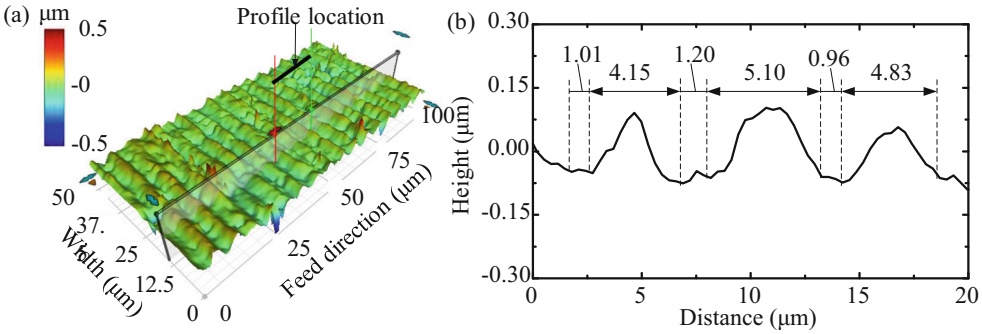

Fig. 16 An unbalanced cutting phenomenon due to the radial runout. **a** The 3D morphology of the milled surface. **b** The extracted profile. (milling conditions: $n = 10{,}000$ rpm, $a_p = 30$ μm, $f_z = 2$ μm/z)

influencing the fidelity of the tool profile transferring to the micromilled surface.

According to the literature, the main influential factors are demonstrated in Fig. 18. Set initial conditions: $f_z = 8$ μm, $r_c = 5$ μm, $\alpha = 5°$, the predicted surface profile is shown in Fig. 18a. It is formed by duplicating the cutting edge on a fixed feed rate. When the radial runout (assuming $r_0 = 2$ μm, $\lambda = 30°$) occurs, a high feed rate and a low feed rate cut the surface alternatively, and the formed profile is shown in Fig. 18b. If the axial runout (assuming $r_a = 0.2$ μm) exists at the same time, the cutting depth varies for the two teeth, and the formed profile is shown in Fig. 18c. Furthermore, if the corner radius increases to 15 μm, the formed profile is shown in Fig. 18d. The predicted roughnesses by the established model indicate that the occurrences of the radial and axial runout increase the surface roughness, while the increase of the corner radius reduces the surface roughness. The influence of the large tool nose radius on surface roughness is verified by Chou et al. [33], who conducted a series of finish turning experiments on the hardened steel.

Except for the influence of radial and axial runout, and the corner radius, as discussed in previous sections, the effects of elastic recovery and swelling, MCT, the waviness of tool cutting edge, and the vibration all play significant roles in the formation process of the surface profile. In terms of the elastic recovery and swelling, as shown in Fig. 18e, the actual surface profile is formed after the material swelling and elastic recovery. To et al. [34], Liu et al. [13], and Sata et al. [35] all demonstrated that the swelling effect could increase the surface roughness since the

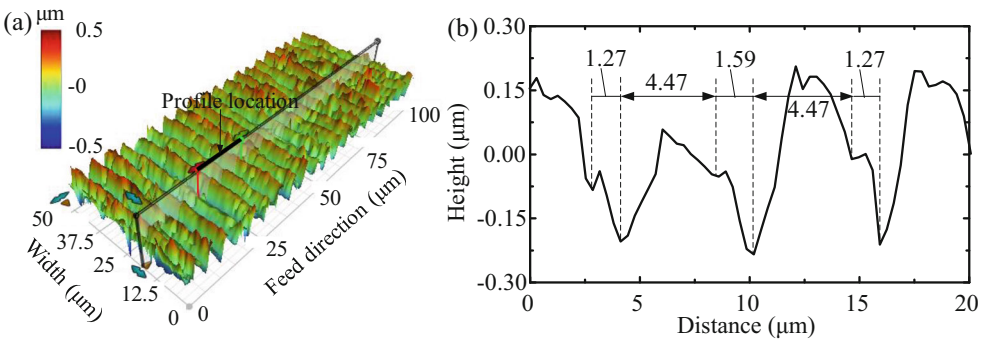

Fig. 17 An unbalanced cutting phenomenon due to the axial runout. **a** 3D morphology. **b** The extracted profile. (milling conditions: $n = 10{,}000$ rpm, $a_p = 30$ μm, $f_z = 3$ μm/z)

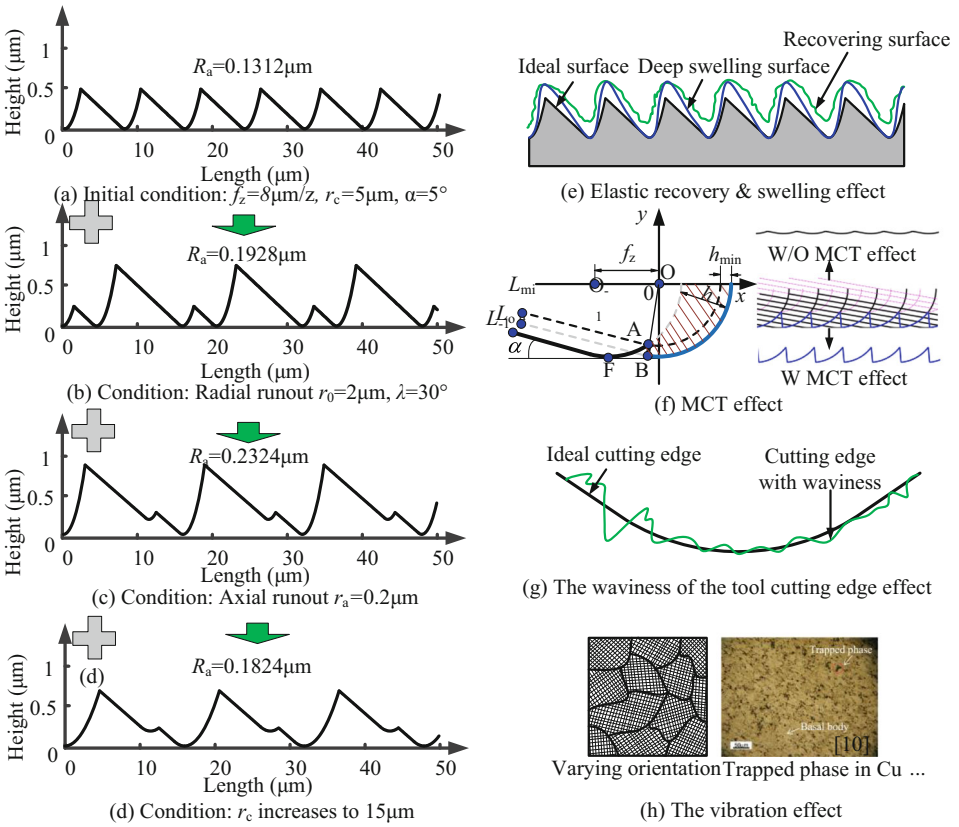

Fig. 18 The main influential factors for micromilled surface morphology. **a** The predicted profile at the initial condition: f_z = 8 μm/z, r_c = 5 μm, α = 5°; **b** plus radial runout r_0 = 2 μm, λ = 30°; **c** plus axial runout r_a = 0.2 μm. **d** r_c increases to 15 μm. **e** Elastic recovery and swelling effect. **f** MCT effect. **g** The waviness of the tool cutting edge effect. **h** The vibration effect

swelling increases the height of the peaks. After the elastic recovery, the variance of the surface roughness depends on the amount of recovery, which is decided by the material properties and forces on the flank face [36]. If the swelling effect is overwhelmed by the effect of material recovery, the surface roughness could decrease [37].

In terms of MCT, since a critical uncut chip thickness exists in the cutting process, under which the material cannot be cut down, thereby leaving on the milled surface and increasing the surface roughness [25]. The typical surfaces formed with and without the effect of MCT are shown in Fig. 18f. As for the waviness of the tool cutting edge, it is usually neglected in the modeling process; however, due to the limitation of the cutting tool fabrication technologies and material properties, the occurrence of tool edge waviness is inevitable [8], as shown in Fig. 18g. Especially, when there is tool wear on the cutting edge, the waviness is supposed to increase dramatically, which will duplicate on the machined surface in the milling process, and influence the surface morphology. As for the vibration during the slot micromilling process, the phenomenon could be caused by cutting across grains [38] or cutting the hard trapped phase and soft basal body alternatively [33], as shown in Fig. 18h. Besides, based on the results from single point diamond turning tests, Tauhiduzzaman et al. [39] found that the grain boundary density also influences the surface roughness. To sum up, in order to obtain a more accurate surface morphology, the more influential factors should be considered in the model.

6 Conclusions

This work aims to reveal the influence of the radial and axial runout and tool corner radius on the slot micromilling process. The main conclusions can be drawn as follows:

1. In terms of the model for predicting uncut chip thickness, the results of Nie's, Bao's, and Wan's model were compared with the result of a numerical calculation method based on the Newton–Raphson (N-R) iterative method. The results indicated that Bao's model had the best accuracy among the three models, which was used to calculate the actual feed rate in the surface morphology modeling.
2. For the influence of r_0 and λ, the surface roughness increased with the radial runout offset. The surface roughness decreased with the increase of runout angle when the runout angle was below 90°, while the scenario reversed when the runout angle is above 90°.
3. For the influence of r_a and r_0, the surface roughness increased with the radial runout offset and axial offset. For the influence of r_a and λ, the minimum surface roughness was around the zone with a low axial runout offset and a

90° radial runout angle. Yellow areas on both contours were not influenced by the runout parameters. The results of the 2D profile analysis indicated that a single tooth cutting phenomenon occurred at those zones.

4. For the influence of r_0 and r_c, the smaller corner radius and larger radial runout offset could obtain higher surface roughness. For the influence of r_a and r_c, the surface roughness increased with the increase of the axial runout offset and the decrease of the corner radius. When the axial runout offset was above 0.2 μm, the influence of axial runout offset vanished, which could also be attributed to the occurrence of a single-tooth cutting phenomenon.
5. From the micromilled surface in the experiment, three typical surface morphologies, i.e., a single cutting phenomenon, unbalanced cutting phenomena due to the radial runout and axial runout, are obtained, which could be successfully explained by the established model. Besides, a new single-tooth cutting criterion was proposed, which could consider the influence of radial and axial runout simultaneously.

Acknowledgments The authors are also grateful to the colleagues for their essential contribution to the work.

Funding information This work is supported by the China Postdoctoral Science Foundation (Grant Nos. 2019M663043), the National Natural Science Foundation of China (Grant Nos. 51575360 and 51805333), and the Science and Technology Innovation Commission Shenzhen (Grant Nos. JCYJ20170817094310049 and JSGG20170824111725200).

References

1. Wojciechowski S, Mrozek K (2017) Mechanical and technological aspects of micro ball end milling with various tool inclinations. Int J Mech Sci 134:424–435
2. Bruschi S, Tristo G, Rysava Z, Bariani PF, Umbrello D, De Chiffre L (2016) Environmentally clean micromilling of electron beam melted ti6al4v. J Clean Prod 133:932–941
3. Yuan Y, Jing X, Ehmann KF, Cao J, Li H, Zhang D (2018) Modeling of cutting forces in micro end-milling. J Manuf Process 31:844–858
4. Liu X, Devor RE, Kapoor SG (2007) Model-based analysis of the surface generation in microendmilling—part i: model development. J Manuf Sci Eng 129(3):461–469
5. Singh D, Rao PV (2007) A surface roughness prediction model for hard turning process. Int J Adv Manuf Technol 32:1115–1124
6. Palanikumar K (2008) Application of Taguchi and response surface methodologies for surface roughness in machining glass fiber reinforced plastics by PCD tooling. Int J Adv Manuf Technol 36:19–27
7. Wang T, Xie LJ, Wang XB, Jiao L, Shen JW, Xu H (2013) Surface integrity of high speed milling of al/sic/65p aluminum matrix composites. Procedia Cirp 8:475–480
8. He CL, Zong WJ, Sun T (2016) Origins for the size effect of surface roughness in diamond turning. Int J Mach Tools Manuf 106:22–42
9. Rahman MA, Amrun MR, Rahman M, Kumar AS (2017) Variation of surface generation mechanisms in ultra-precision machining due to relative tool sharpness (RTS) and material properties. Int J Mach Tools Manuf 115:15–28
10. Chen J, Zhao Q (2015) A model for predicting surface roughness in single-point diamond turning. Measurement 69:20–30
11. Lee WB, Cheung CF (2001) A dynamic surface topography model for the prediction of nano-surface generation in ultra-precision machining. Int J Mech Sci 43(4):961–991
12. Wang H, To S, Chan CY, Cheung CF, Lee WB (2010) A theoretical and experimental investigation of the tool-tip vibration and its influence upon surface generation in single-point diamond turning. Int J Mach Tools Manuf 50(3):241–252
13. Liu K, Melkote SN (2006) Effect of plastic side flow on surface roughness in micro-turning process. Int J Mach Tools Manuf 46(14):1778–1785
14. Zong WJ, Huang YH, Zhang YL, Sun T (2004) Conservation law of surface roughness in single point diamond turning. Int J Mach Tools Manuf 84:58–63
15. Wojciechowski S, Matuszak M, Powałka B, Madajewski M, Maruda RW, Krolczyk GM (2019) Prediction of cutting forces during micro end milling considering chip thickness accumulation. Int J Mach Tools Manuf 147:103466
16. Oliveira FB, Rodrigues AR, Coelho RT, Souza AF (2015) Size effect and minimum chip thickness in micromilling. Int J Mach Tools Manuf 89:39–54
17. Jing X, Tian Y, Yuan Y, Wang F (2017) A runout measuring method using modeling and simulation cutting force in micro end-milling. Int J Adv Manuf Technol 91(9–12):4191–4201
18. Zhang X, Zhang J, Zhang W, Li J, Zhao W (2018) A non-contact calibration method for cutter runout with spindle speed dependent effect and analysis of its influence on milling process. Precis Eng 51:280–290
19. Attanasio A (2017) Tool run-out measurement in micro milling. Micromach 8(7):221
20. Li K, Zhu K, Mei T (2016) A generic instantaneous undeformed chip thickness model for the cutting force modeling in micromilling. Int J Mach Tool Manu 105:23–31
21. Zhang X, Ehmann KF, Yu T, Wang W (2016) Cutting forces in micro-end-milling processes. Int J Mach Tool Manu 107:21–40
22. Sun Y, Liang Y, Du R (2006) Simulation and analysis of surface generation in micro-milling. In Proceedings of the 6th WSEAS International Conference on Robotics, Control and Manufacturing Technology, Hangzhou, China (pp. 30-35)
23. Li H, Lai X, Li C, Feng J, Ni J (2007) Modeling and experimental analysis of the effects of tool wear, minimum chip thickness and micro tool geometry on the surface roughness in micro-end-milling. J Micromech Microeng 18(2):025006
24. Kim GH, Yoon GS, Lee JW, Kim HK, Cho MW (2012) A study on the micro-endmilling surface prediction model with non-dynamic errors. Int J Precis Eng Manuf 13(11):2035–2041
25. Chen W, Huo D, Teng X, Sun Y (2017) Surface generation modeling for micro end milling considering the minimum chip thickness and tool runout. Procedia CIRP 58:364–369
26. Chen W, Sun Y, Huo D, Teng X (2019) Modeling of the influence of tool runout on surface generation in micro milling. Chin J Mech Eng 32(1):2
27. Aurich JC, Bohley M, Reichenbach IG, Kirsch B (2017) Surface quality in micro milling: influences of spindle and cutting parameters. CIRP Ann-Manuf Techn 66:101–104
28. Nie Qiang (2015) Modeling and process research of micro cutting technology. Shanghai Jiao Tong University, Master Dissertation
29. Bao WY, Tansel IN (2000) Modeling micro-end-milling operations. Part II: tool run-out. Int J Mach Tool Manu 40(15):2175–2192
30. Wan M, Zhang WH, Dang JW, Yang Y (2009) New procedures for calibration of instantaneous cutting force coefficients and cutter

runout parameters in peripheral milling. Int J Mach Tool Manu 49(14):1144–1151
31. Afazov SM, Ratchev SM, Segal J, Popov AA (2012) Chatter modeling in micro-milling by considering process nonlinearities. Int J Mach Tool Manu 56:28–38
32. Kuram E, Ozcelik B (2016) Micro-milling performance of aisi 304 stainless steel using taguchi method and fuzzy logic modeling. J Intell Manuf 27(4):817–830
33. Chou YK, Song H (2004) Tool nose radius effects onfinish hard turning. J Mater Process Technol 148:259–268
34. To S, Cheung CF, Lee WB (2001) Influence of material swelling upon surface roughness in diamond turning of single crystals. Mater Sci Technol 17(1):102–108
35. Sata T, Li M, Takata S, Hiraoka H, Li QQ, Xing XZ, Xiao XG (1985) Analysis of surface roughness generation in turning operation and its applications. Ann CIRP 34:473–476
36. Cheung CF, Lee WB (2000) A multi-spectrum analysis of surface roughness formation in ultra-precision machining. Precis Eng 24: 77–87
37. Kong MC, Lee WB, Cheung CF, To S (2006) A study of materials swelling and recovery in single-point diamond turning of ductile materials. J Mater Process Technol 180:210–215
38. Xie L, Shang T, Chen X, Zheng M, Zhang L, Qin Y (2016) Comparative investigation on microstructure-based modeling for the orthogonal cutting of aisi1045. Int J Adv Manuf Technol 88(1):1–9
39. Tauhiduzzaman M, Veldhuis SC (2014) Effect of material microstructure and tool geometry on surface generation in single point diamond turning. Precis Eng 38:481–491